

Surface Asymmetry of Coated Spherical Nanoparticles

Amelie H. R. Koch,[†] Gaëtan Lévêque,[‡] Sebastian Harms,[§] Karmena Jaskiewicz,[†] Max Bernhardt,[†] Andreas Henkel,[§] Carsten Sönnichsen,[§] Katharina Landfester,[†] and George Fytas^{†,‡,*,#}

[†]Max Planck Institute for Polymer Research, Ackermannweg 10, 55128 Mainz, Germany

[‡]Institut d'Électronique, de Microélectronique et de Nanotechnologie (IEMN), UMR-CNRS 8520, UFR de Physique, Université de Lille 1, 59655 Villeneuve d'Ascq, France

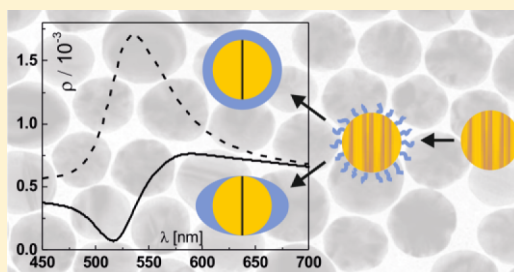
[§]Institut für Physikalische Chemie, Johannes Gutenberg Universität, Duesbergweg 10-14, 55128 Mainz, Germany

[#]Department of Materials Science, University of Crete and IESL/FORTH, 71110 Heraklion, Greece

S Supporting Information

ABSTRACT: We validate the nonspherical grafting arrangement of isotropically coated spherical nanoparticles as very recently proposed. We utilize localized surface plasmon resonance enhanced dynamic polarized and depolarized light scattering from Au nanoparticles, the spherical symmetry of which was revealed by single-particle dark-field spectroscopy. The same Au nanospheres are grafted with ligands of different chemistry and length. The wavelength dependent depolarization ratio and the two transport coefficients of these nanoparticles, obtained from the dynamic light scattering experiment, can only be reconciled with the TEM data, the single UV/vis extinction spectrum, and the dark-field spectroscopy experiments if their coating is described as asymmetric. Spatially anisotropic graft distribution on spherical nanoparticles impacts their assembly and understanding its origin will help control the structure and properties of polymer nanocomposites.

KEYWORDS: Plasmonics, grafted gold nanospheres, depolarized light scattering, shape anisotropy, nanospheres, extinction



Inorganic nanoparticles or nanocrystals produced by wet-chemical synthesis offer potential solutions to many aspects of nanoscience from biomedicine, optics, and electronics to sensing.^{1–5} Integrating such nanoparticles into new materials requires their chemical stabilization against uncontrolled aggregation and in most cases further chemical functionalization to direct their self-assembly into the desired structures.⁶ Initially, stabilization of nanoparticles (NPs) is often achieved by electrostatic repulsion. However, handling is greatly improved by steric and entropic stabilization with short-chain polymers that allow stabilization against salt, temperature, and even drying.^{7,8} Uncharged uniformly coated NPs are, for example, valuable additives that can enhance the physical properties of polymer nanocomposites. The dispersion of NPs in polymeric materials is, however, difficult and by far not understood.^{9,10} Even for spherical shape particle grafts, the dispersion frequently results in agglomeration into anisotropic structures^{11–13} such as strings resembling the behavior of patchy NPs.¹⁴ This observation is counterintuitive in view of both spherically symmetric particle shape and isotropic interactions. Very recent computer simulations^{15–17} have shown that the organization of grafts around spherical NPs can deviate from spherical symmetry producing asymmetric configurations for otherwise isotropically grafted NPs. The organization of grafts can be of inherent origin,¹⁷ driven by fluctuations, and of adherent origin^{15,16} due to the interplay of graft–solvent interactions. An important parameter for this anisotropic distribution of grafts is the excess volume explored

per graft on a sphere relative to flat surface of the same area. An experimental validation of this peculiar geometry-induced grafted particle shape anisotropy is missing.

In this Letter, we investigate the shape of NPs consisting of spherical Au cores stabilized by chains with different chemistry and length for two core diameters in very dilute aqueous dispersions by dynamic polarized and depolarized light scattering, UV/vis extinction and single-particle dark-field spectroscopy. The system and the methods were selected on account of the sensitivity of the depolarized scattering, which is localized surface resonance (LSPR) enhanced,¹⁸ to deviations from spherical symmetry and the strong dependence of the LSPR frequency of the Au core on orientation and local environment.¹⁹ In addition, LSPR-enhancement is wavelength dependent and the depolarized light scattering inherent to the spherical bare AuNPs is not zero due to the inevitable internal crystallinity.^{20,21} All experimental static and dynamic quantities that include the wavelength-dependent depolarization ratio, LSPR spectrum, and two transport coefficients can be consistently described only if particle shape anisotropy is assumed.

The virtually spherical shape of two bare gold nanoparticles (AuNPs) synthesized (Supporting Information S1) for the

Received: May 13, 2014

Revised: June 12, 2014

Published: June 13, 2014

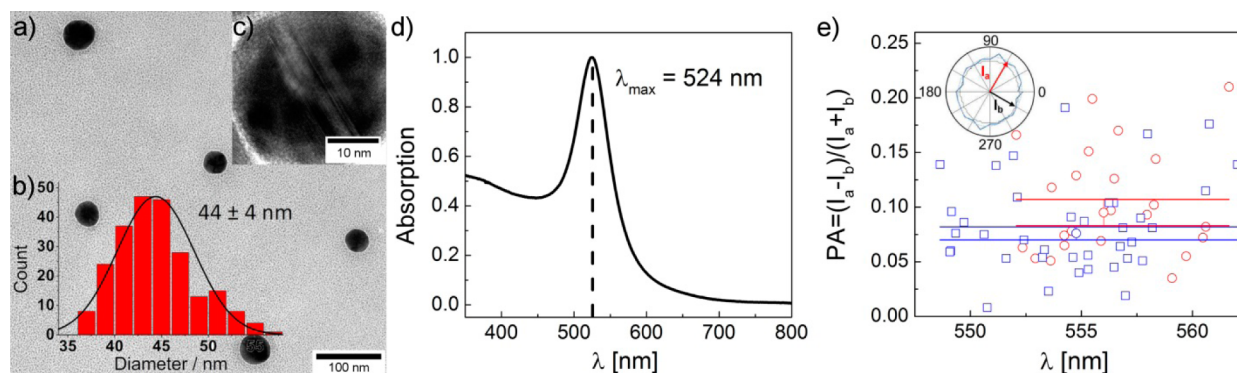


Figure 1. (a) TEM image of AuNPs, (b) size-distribution, (c) high-resolution TEM image of a single AuNP, and (d) the localized surface plasmon resonance peak in the extinction spectrum of dilute suspension of AuNPs stabilized with citrate. (e) Polarization anisotropy measured by single-particle dark-field spectroscopy shows similar asphericities for Au-citrate (red circles) as well as Au-PEG₁₀₇ (blue squares).

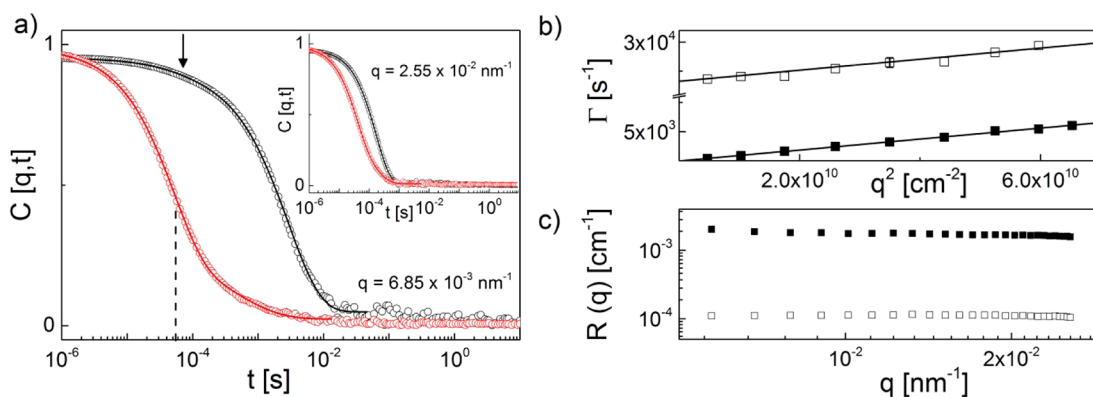


Figure 2. (a) Relaxation functions [$C_{VV}(\mathbf{q},t)$, $C_{VH}(\mathbf{q},t)$] for a dilute ($c = 0.01 \text{ g L}^{-1}$; $cM = 0.02 \text{ nM}$) aqueous suspension of Au nanospheres (diameter $d = 44 \text{ nm}$) stabilized with citrate at the scattering wave vector $\mathbf{q} = 6.85 \times 10^{-3} \text{ nm}^{-1}$ (corresponding to a diffusion length $\sim 920 \text{ nm}$), recorded for VV (black symbols) and VH (red circles) polarizations. The solid lines indicate the theoretical representation (see text) of the experimental functions and the arrow denotes the fast VH contribution to $C_{VV}(\mathbf{q},t)$. (b) The relaxation rate Γ_s (solid squares) for the slow (VV) and Γ_f (open squares) for the fast (VH) component in $C_{VV}(\mathbf{q},t)$ and $C_{VH}(\mathbf{q},t)$, respectively. (c) Time-average absolute Rayleigh ratio for polarized $R_{VV}(\mathbf{q})$ (solid squares) and depolarized $R_{VH}(\mathbf{q})$ (open squares) light scattering for the same Au nanospheres solution versus \mathbf{q} . The PCS experiment was performed with coherent laser light at $\lambda = 632 \text{ nm}$ above λ_{max} ($\sim 524 \text{ nm}$) of the extinction spectrum (Figure 1d).

scope of this study was revealed by transmission electron microscopy (TEM) and single particle polarization anisotropy (PA) experiments (Supporting Information S2)^{22,23} and supported by the extinction spectrum in dilute aqueous solutions. TEM images (Supporting Information S3) for the AuNPs with the thinnest (citrate) coating shows the size distribution with an average $44 \pm 4 \text{ nm}$ diameter (Figure 1a,b) and reveals the crystalline nature of individual AuNPs at high-resolution TEM (Figure 1c). Polycrystallinity^{21,24,25} turns out to be crucial for the behavior of electrons and twinning defects can impact the optical properties as discussed below.

The single peak in the extinction spectrum of Au-citrate NPs (Figure 1d and Supporting Information S4) conforms to the spherical symmetry of the Au core displaying only one LSPR mode. For the latter, however, a quantitative measure of the asphericity is obtained by the PA experiment using Au-citrate and Au-PEG₁₀₇ where AuNPs are grafted with poly(ethylene glycol) (PEG) chain of about 107 ethylene glycol units (Figure 1e). The pattern of the polarization anisotropy of the scattering intensity from individual Au cores reveals a virtually spherical shape with aspect ratio of 1.029 and 1.023 for citrate- and PEG-coated particles respectively, which were calculated from the polarization anisotropy. Since the grafts are not visible in the TEM images and PA experiment, deviations from the spherical

symmetry revealed below can be ascribed only to asymmetric graft arrangements.

For Au nanorods, dynamic depolarized light scattering is significantly enhanced near the longitudinal SPR frequency¹⁸ but for plasmonic nanospheres with a single LSPR mode this information is still missing. Since anisotropic dynamic light scattering is also anticipated for spherical NPs due to inherent crystallinity,²⁰ we employ photon correlation spectroscopy (PCS) both polarized (VV) and depolarized (VH) (Supporting Information S5) for the first experimental report on shape and transport coefficients of grafted Au nanospheres. The absolute polarized $R_{VV}(\mathbf{q})$ and depolarized $R_{VH}(\mathbf{q})$ are shown as a function of the scattering wave vector \mathbf{q} for a 0.02 nM Au-citrate solution in Figure 2c; $R_{VH}(\mathbf{q})$ is virtually flat, while $R_{VV}(\mathbf{q})$ exhibits a weak \mathbf{q} -dependence due to the small particle size (Guinier plot in Supporting Information Figure S1a). Unexpectedly, the depolarization ratio $\rho = R_{VH}/R_{VV}$ (about 7%) is very high considering the spherical shape of the Au core. It therefore allows us to record the orientation relaxation function $C_{VH}(\mathbf{q},t)$ that exhibits a single exponential decay with relaxation rate $\Gamma_{VH}(\mathbf{q}) = 6D^r + \mathbf{q}^2 D^t$ (Figure 2a, b), where D^r and D^t denote the rotational and translational diffusion coefficients. For fast $D^r (> \mathbf{q}^2 D^t)$, the estimation of D^t from the slope of $\Gamma_{VH}(\mathbf{q})$ is subject to large error. Hence it is obtained from the

$C_{VV}(\mathbf{q}, t)$ which in all known cases but plasmonics is a single decay function with a relaxation $\Gamma_{VV}(\mathbf{q}) = \mathbf{q}^2 D^t$. For noble metal NPs, however, the anisotropic R_{VH} is LSPR-enhanced and hence its contribution in $C_{VV}(\mathbf{q}, t) = a_{VH} \exp(-\Gamma_{VH} t) + a_{iso} \exp(-D^t \mathbf{q}^2 t)$ can be discernible as a second fast decay (arrow in Figure 2a) with amplitude a_{VH} ; for Au nanorods with comparable amplitudes, the two-step decay of $C_{VV}(\mathbf{q}, t)$ becomes very pronounced.¹⁸ The slow purely isotropic component with amplitude a_{iso} decays via translational diffusion allowing a precise determination of D^t from the slope of the linear dependence, $\Gamma_{VV}(\mathbf{q}) = \mathbf{q}^2 D^t$ (Figure 2b). The consistent representation of $C_{VH}(\mathbf{q}, t)$ and $C_{VV}(\mathbf{q}, t)$ is also indicated by the same slope of $\Gamma_{VH}(\mathbf{q})$ and $\Gamma_{VV}(\mathbf{q})$ in Figure 2b. The transport coefficient D^t is directly obtained from the intercept of the rate $\Gamma_{VH}(\mathbf{q} \rightarrow 0)$.

The comprehensive PCS experiment yields the transport coefficients, D^t and D^r , and the depolarization ratio, ρ , measured for seven different grafts of the same Au core at 532 nm, near the peak position (λ_{max}) of the LSPR mode, and 632 nm representing off resonance conditions. From D^t and D^r , we compute the hydrodynamic radius $R_h = k_B T / (6\pi\eta_s D^t)$ and the rotational radius $R_r = [k_B T / (8\pi\eta_s D^r)]^{1/3}$ for a sphere under stick boundary conditions, where k_B is the Boltzmann's constant and η_s the solvent viscosity. In the opposite case of slip boundary conditions, R_h and in particular R_r would assume unacceptable much higher values in order to conform to the two experimental transport coefficients.^{26,27} Moreover, the grafting of the particles should enhance interactions between surface and the surrounding solvent and stick boundary conditions are therefore more plausible. Table 1 summarizes

Table 1. Characteristic Dimensions of Au Nanospheres with Adsorbed Citrate or Different Grafted Chains, Depolarization Ratio at Two Optical Wavelengths, and the Wavelength of the Single Surface Plasmon Resonance

	R_h [nm]	R_r [nm]	$\rho = R_{VH}/R_{VV}$		λ_{max} [nm]
			632 nm	532 nm	
Au-citrate	23.7 ± 0.5^a	34.8 ± 0.7	0.07	0.01	524
Au-PEG ₁₆	27.3 ± 0.4^b	36.8 ± 0.7	0.03	0.01	524
Au-PEG ₄₅	31.4 ± 0.5^b	40.0 ± 2	0.04	0.02	525
Au-PEG ₁₀₇	37.0 ± 1.4^b	40.0 ± 0.6	0.02	0.01	525
Au-PEG _{107-COOH}	37.1 ± 0.4^b	44.0 ± 1.3	0.03	0.01	525
Au-DNA _{T10}	32.0 ± 1.9	42.0 ± 2.1	0.01	0.01	526
Au-DNA _{T40}	36.5 ± 0.5	42.0 ± 1.4	0.01	0.01	526

^aFor Au-citrate, $2R_h \approx d$ from TEM. ^bFor Au-PEG_N, the layer thickness $\Delta R_h = (2R_h - d) \sim N^{0.6}$ (Supporting Information Figure S1b)

the sizes (R_h , R_r), the depolarization ratio at two irradiation laser wavelengths and the position of LSPR peak for very dilute suspensions of the same AuNP core (with diameter $d = 44$ nm) bearing seven different coatings. The scaling of the layer thickness for the PEG-grafted Au nanospheres, $\Delta R_h = (2R_h - d) \sim N^{0.6}$ (Supporting Information Figure S1b) with the PEG degree of polymerization, N , implies swollen chain configurations. The absolute Rayleigh scattering intensities, R_{VV} and R_{VH} , are stronger near resonance ($\lambda = 532$ nm) but exhibit a different drop at $\lambda = 632$ nm, as seen in Figure 3a. Consequently, the polarization ratio depends on λ , but surprisingly ρ assumes a larger value at $\lambda = 632$ nm, that is, at off-resonance (Figure 3b, Table 1); the highest value is

observed for the citrate and the lowest for the DNA coatings. The experimental quantities, intensities, depolarization ratio, and the ratio of the two transport coefficients, assume the same values at 20 and 50 °C.

Two unexpected findings are emphasized: (i) $R_r > R_h$ for all examined AuNPs (Table 1) and (ii) the value of ρ varies from 0.01 to 0.07 depending on the wavelength λ of the illuminated light and the grafted layer on the same Au core. For all grafts, ρ is stronger when λ is off resonance (at 632 nm) (Figure 3b) due to the different λ -dependence of the R_{VV} and R_{VH} intensities (Figure 3a). This behavior was also found for a different Au core ($d = 41$ nm) also with chemically different grafts (Supporting Information Figure S2).

First, we discuss the finite value and the λ -dependence of the depolarization ratio with analytical and numerical models described in the Supporting Information (S6–S9). Because for AuNPs of spherical shape $\rho = 0$, we start with the predicted behavior for a spheroidal “monocrystalline” Au cores using the Green’s tensor method (Supporting Information S6). The length ratio, b/a , of the particle main axis (b) to the perpendicular degenerated axis (a) is allowed to slightly vary around one according to the single-particle dark-field microscopy results (Figure 1e) but considering also a size distribution with a width Δb . The experimental condition of a single peak extinction spectrum (Figure 1d) sets the upper bound of the ratio $\Delta b/b \sim 10\%$ as suggested by the distribution obtained from the TEM images (Figure 1b). Spheroids with this size distribution, however, can neither reach the experimental depolarization ratio values, nor predict the experimentally observed higher value of the depolarization ratio at off-resonance. This opposite trend in the theoretical calculations is demonstrated in Figure 4a. While the maximum value of ρ expectedly increases with $\Delta b/b$, it occurs near resonance (~ 550 nm) and its value even for an aspect ratio ~ 1.1 remains well below the experimental value.

To boost the value of ρ and predict an off-resonance enhancement, we introduce next “polycrystallinity” in an analytical model, which is the origin for the present nonzero depolarized light scattering from spherical Au cores. Crystallinity characterization is a challenging issue and can benefit from the study of twinning defects on the properties of plasmonic NPs. The splitting of the quadrupolar vibration mode in the low-frequency Raman spectrum²¹ due to LSPR-acoustic coupling was related to the crystallinity of an ensemble of AuNPs. Here, we relate nanocrystallinity to the anisotropic optical properties due to anisotropic electron free paths. More precisely, the effect of a cut plane between two monocrystals is modeled as an increased absorption rate of the free electrons in gold colliding with the cut plane, resulting in a shortened mean free path for the electrons moving perpendicular to the cut compared to the electrons moving parallel to it. Such a model is often used to describe the increased absorption in metal nanoparticles of size shorter than the mean free path of the free electrons in the bulk metal.²⁸

Hence, a basic phenomenological model for the Au-polycrystallinity has been implemented in the theoretical calculations (Supporting Information S7). The polycrystalline particle is described as a spherical or spheroidal particle cut into several parallel slices of equal thickness l , along the direction of one of the principal axes, as shown in Supporting Information Figure S3. Each cut plane between two slices behaves as a barrier whose effect is to increase the collision rate of electrons moving perpendicularly to it by a factor inversely proportional

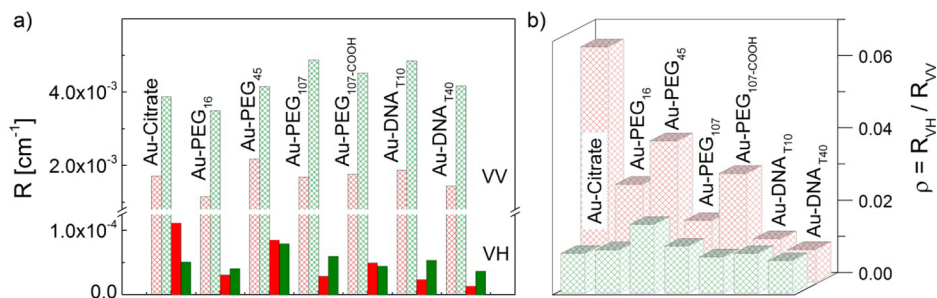


Figure 3. (a) Absolute Rayleigh ratio for polarized (R_{VV} , hatched areas) and depolarized (R_{VH} , solid areas) light scattering and (b) depolarization ratio ρ at 532 nm (green) and 632 nm (red) for a dilute suspension of Au nanospheres with 44 nm diameter core and different grafts as indicated in the plots.

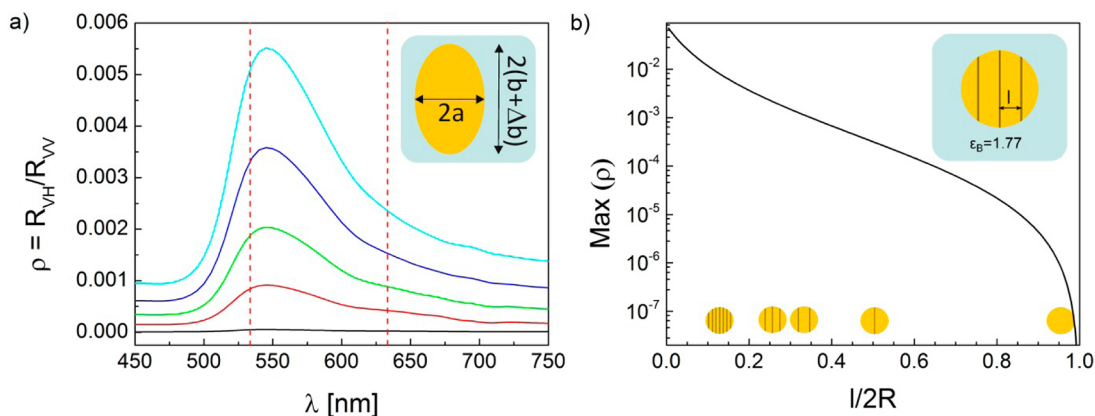


Figure 4. (a) Calculated depolarization ratio ρ for spheroidal AuNPs in the presence of size distribution and different shapes in the range $0 \leq \Delta b/b \leq 10\%$ ($\Delta b/b = 2\%$ (black), $\Delta b/b = 4\%$ (red), $\Delta b/b = 6\%$ (green), $\Delta b/b = 8\%$ (blue), $\Delta b/b = 10\%$ (cyan)). The two vertical lines denote the wavelengths of the lasers employed in the experiment. The maximum depolarization ratio (at about 550 nm) increases with the asphericity $\Delta b/b$. (b) Effect of polycrystallinity modeled by anisotropic absorption, that is, anisotropic electron mean free path l .

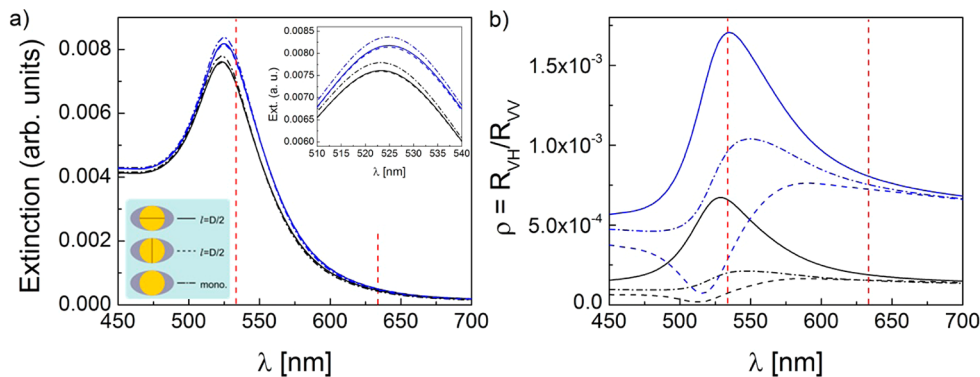


Figure 5. (a) Computed extinction spectra for polycrystalline Au nanosphere ($d = 44$ nm) coated with a nonspherical shell ($a' = 0$ nm, $b' = 10$ nm) and two different refractive indices ($n_{\text{graft}} = 1.41$, black; $n_{\text{graft}} = 1.5$, blue). The inherent Au anisotropy direction, perpendicular to the cut plane (the line in the gold core) inside the AuNP, is either perpendicular (solid lines) or parallel (dashed lines) to the graft anisotropy axis while the dot-dashed line is for monocrystalline AuNPs. (b) Depolarization ratio for the three polycrystallinity configurations and the two graft refractive indices in (a) as a function of the light wavelength; note the inversion of ρ (532 nm)/ ρ (632 nm) between perpendicular (solid lines) and perpendicular parallel (dashed lines) anisotropy directions. The two vertical dashed lines denote the wavelength of the two lasers employed in the experiment.

to the slice thickness; for n cuts (n being called in the following the degree of polycrystallinity), $l = 2R/(n + 1)$. This introduces an anisotropic electron mean free path. Electrons moving normal to the cut planes have a shorter mean free path on the order of l compared to $2R$, when the electrons are moving along one of the two other directions parallel to the cut planes. Consequently, the light absorption for polarization perpendicular to the cut plane will be larger than for light polarized along the two other directions. In the following, the former is called

the inherent Au anisotropy. Hence the anisotropic absorption renders the depolarization ratio of an otherwise spherical shape higher.

Using an analytical expression of the depolarization ratio (Supporting Information S8), we show that the value of ρ at maximum ($\lambda \sim 550$ nm) of Au nanospheres increases rapidly for $l/2R < 1$ and $\rho \sim 0.01$ can be formally captured for $l/2R \sim 0.05$ as seen in Figure 4b. In this model, a symmetric coating of the Au nanosphere, that is, a spherical core–shell particle, fails

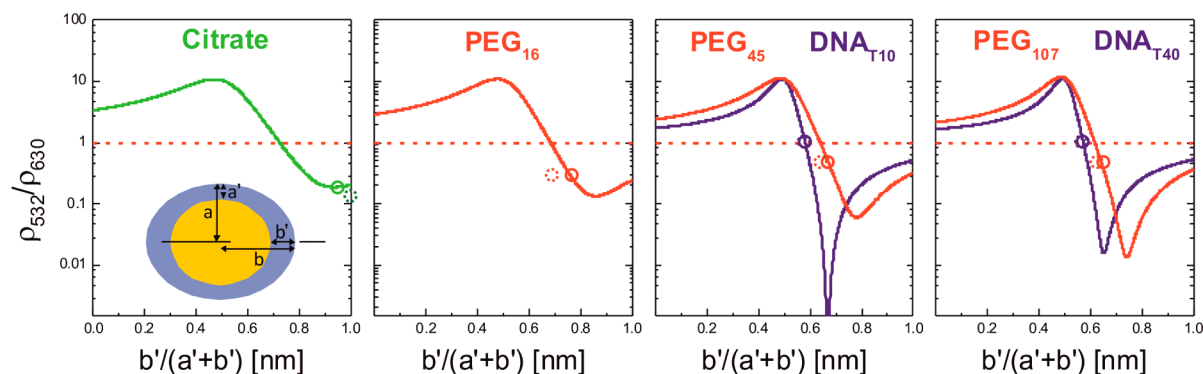


Figure 6. Comparison between the experimental asphericity parameter $b'/(a' + b')$ (dashed circles) with the corresponding computed (solid circles) $b'/(a' + b')$ for the same AuNP with six different coatings using core of diameter $d = 44$ nm and the $\rho^* = \rho(532 \text{ nm})/\rho(632 \text{ nm})$ values from Table 2.

Table 2. Refractive Indexes n_{graft} of the Different Coatings, Experimental (from Supporting Information Table S3 in bold) and Theoretical Values of a' , b' , $b'/(a' + b')$ and ρ^*

	n_{graft}	a' [nm]	b' [nm]	$b'/(a' + b')$	ρ^*				
Au-citrate	1.50	0.0	0.5	6.6	6.1	1.00	0.93	0.14	0.19
Au-PEG ₁₆	1.46	3.7	3.1	8.8	9.4	0.70	0.75	0.33	0.33
Au-PEG ₄₅	1.46	7.5	6.9	13.4	14.0	0.64	0.67	0.50	0.50
Au-PEG ₁₀₇	1.46	12.7	11.6	19.6	20.7	0.61	0.64	0.50	0.50
Au-PEG _{107-COOH}	1.46	12.9	11.5	19.9	21.3	0.61	0.61	0.33	0.33
Au-DNA _{T10}	1.60	9.0	9.1	12.1	12.0	0.57	0.57	1.00	1.00
Au-DNA _{T40}	1.60	13.0	12.7	16.5	16.8	0.56	0.56	1.00	1.00

to predict the experimental $\rho(532 \text{ nm}) < \rho(632 \text{ nm})$ trend, irrespectively of the values of the adjustable parameters, which in this case are the shell refractive index and the degree n of polycrystallinity. Instead, $\rho(532 \text{ nm})$ is an order of magnitude larger than $\rho(632 \text{ nm})$ for symmetric coatings of spherical Au cores Supporting Information (Figure S4b). More generally, we have verified with this analytical model that an even coating around a spheroidal polycrystalline gold core systematically leads to $\rho(532 \text{ nm}) \geq \rho(632 \text{ nm})$, the equality occurring for slightly prolate Au NP with a polycrystallinity degree $n = 2$ (not shown). Similarly, combining polycrystallinity with slightly prolate or oblate AuNPs without any shell fails to reproduce the lower depolarization ratio at the plasmon resonance. Assuming, however, an asymmetric arrangement of grafts in the theoretical calculations, the behavior can be reversed.

The graft is characterized by its thickness b' along the particle revolution axis, and a' along the two perpendicular degenerated axes. The extinction spectrum and the depolarization ratio for two graft arrangements in Figure 5 show that the depolarization ratio can be lower at resonance when the shell anisotropy is directed normal to the cut plane inside the AuNP, that is, parallel to the inherent Au anisotropy direction (dashed lines in Figure 5); calculations for different b' values are presented in Supporting Information Figure S4. The extinction spectrum retains its single peak shape in agreement with the experiment apart from subtle frequency shift (inset to Figure 5a). For “monocrystalline” Au core, ρ , caused by the imposed asymmetric grafting, is increased while it assumes the highest value at resonance. Finally, the strongest depolarization ratio is obtained when the grafting and inherent anisotropy directions are perpendicular to each other, and again reaches the largest value at resonance. Quantitatively, the displayed behavior in Figure 5 depends on the assumed refractive index n_{graft} of the grafted layer and the effect is more pronounced for high n_{graft} .

A quantitative representation of the experimental ρ and the ratio $\rho^* = \rho(532 \text{ nm})/\rho(632 \text{ nm}) \leq 1$ depends on the geometrical parameters (a' , b'), polycrystallinity (n), dielectric constants of Au core and hydrated grafts. Using the analytical model described in Supporting Information S8, we deliberately fixed the core shape to a sphere ($a = b$) as asphericity is experimentally shown to be very small (Figure 1e), the polycrystallinity parameter n to 2, the sum $a' + b'$ to the value deduced experimentally (see Supporting Information Table S3) for every type of grafting. We have then varied the asphericity parameter $b'/(a' + b')$ from zero to one with the case $b'/(a' + b') = 0.5$ corresponding to an even coating of the gold core.

Figure 6 shows the theoretical prediction for the evolution of ρ^* with $b'/(a' + b')$ for the six grafts on the Au core ($d = 44$ nm). The experimental points have been obtained by matching the experimental value of ρ^* with the theoretical curve (solid circles). In any case, the obtained theoretical values for $b'/(a' + b')$ are very close to the experimental one. Notice that for the citrate shell, the experimental value of ρ^* is about 30% lower than the theoretical prediction, however, the minimum is obtained for $b'/(a' + b') \approx 0.93$ (or $a' \approx 0$), which is consistent with the experiment (Supporting Information Table S3). The AuNPs stabilized with citrate, which is, unlike the PEG and DNA grafts, not covalently bonded, exhibit the strongest asphericity.

Table 2 lists the parameters used in the calculations (shell refractive index n_{graft} and $a' + b'$ deduced from the experiment (Supporting Information Table S3)) and the results of the experimental (bold) and theoretical comparison. We note that these values also represent well the two transport coefficients as described below. For all six grafts, $\rho^* \leq 1$ for $0.6 < b'/(a' + b') < 1$, which corresponds to an asymmetric coating configuration. Since the grafting density can vary among the six systems, an

account for the observed differences in the anisotropic coatings is not straightforward. For example, the lowest ρ^* , corresponding to the largest asphericity, was observed for citrate grafts on two different Au cores (Figure 6, Table 1 and Supporting Information Table S1). The exact coverage of the grafts on the particles could not be obtained due to the minute quantity of the samples. We should also note that migration of the thiols on Au surfaces²⁹ is not considered in the calculations, as the extent of this effect is still in dispute.³⁰

Based on recent computer simulations,^{15–17} the asymmetric graft arrangements around spherical NPs depend mainly on grafting density, core to shell sizes, and strength of interactions with the solvent. Qualitatively, low grafting density and long grafts promote NP anisotropy at constant core size. The simulations mostly take into account the graft length, but the density is difficult to include in the model. However, as the largest shell anisotropy has been obtained for citrate, which is not covalently bonded to the Au core, we have to suppose that the distribution of citrate around the shell is very sparse. On the other hand, the correlation between inherent and grafting anisotropy directions (Figure 5) suggested from the theoretical calculations (Supporting Information S7) emphasizes the role of NP's crystallinity. We note that a uniform coating was assumed in the simulation papers.^{15–17}

Second we address the two transport coefficients utilizing the structural information obtained from the representation of ρ^* data. We recall (Table 1) that $R_h < R_r$ is not compatible with spherical symmetry of the Au NPs. Instead, implementation of anisotropic graft shape is also found to account for the difference between the two radii. For an adequate description of D^f by Perrin's equations (Supporting Information S.9), the hydrodynamic volume, $V_h = \kappa V_o$, should exceed ($\kappa \geq 1$) the geometrical volume $V_o = (4/3)\pi p a^3$ with $p = b/a$ being the aspect ratio. Since V_h is not accessible experimentally, the dimensionless κ is treated as an adjustable parameter together with the length b for the long spheroidal axis. For the short axis, the length a is well captured by the experimental hydrodynamic radius, R_h . More specifically, using $a = 0.95R_h$, the two adjustable parameters b and κ were then obtained from the representation of D^t and D^f for all six systems. Figure 7 illustrates exemplarily the followed procedure in the case of Au-PEG₁₆ for which $p \approx 1.2$ and $\kappa = 2.35$. Supporting Information Table S3 summarizes the values for the other systems as well. The value of κ is found to be large for thin shells and

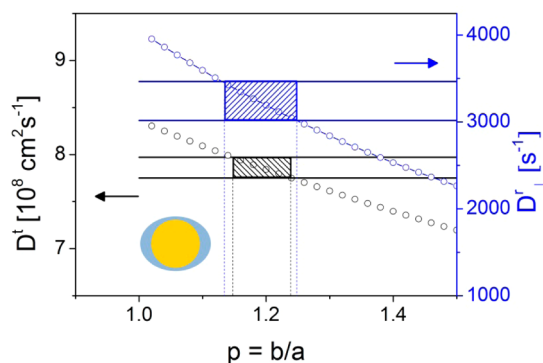


Figure 7. Computed D^t (black) and D^f (blue) for Au-PEG₁₆ using Perrin's eqs (Supporting Information S9) for spheroidal shape is plotted versus aspect ratio, p . The shaded black and blue rectangles represent the experimental range of D^t and D^f respectively.

approaches asymptotically unity for long grafts (Supporting Information Figure S5), that is, $V_h \approx V_o$.

Interestingly, while the bare Au cores assume an almost spherical shape (Figure 1e), the assigned asphericity occurs upon their soft grafting. This is the first experimental report on shape anisotropy of uniformly coated spherical particles, which according to recent simulations can be fluctuation induced¹⁷ or solvent-coating interactions¹⁵ mediated. On the basis of the theoretical representation of the present experimental results, the shell asphericity is parallel to the inherent, due to polycrystallinity, core anisotropy. According to theory and simulations of thiolate-protected gold surfaces,³¹ it is conceivable that different Au outer facets with different binding energies can drive the organization of self-assembled monolayers, that is, the reactivity of (111) facets is lower than of (110) surfaces.³² Noticeably, the present equilibrium configurations are robust to temperature variation between 20 and 50 °C. Because this inherent core effect was not considered in the simulations of the shape of coated NPs,^{15–17} the present experimental work opens a new pathway for engineering the shape of metallic NPs driven by their nanocrystallinity. Access to the Au core nanocrystallinity defects is important because many physical properties such as reactivity and mechanical strength are dependent on whether the metal NPs are 100% single crystalline or 100% twinned.²⁵ On the other hand, control of the overall shape of the same spherical NPs by grafting impact their morphology in polymer nanocomposites.¹¹

■ ASSOCIATED CONTENT

📄 Supporting Information

Detailed description of the preparation and characterization methods and on the theory. This material is available free of charge via the Internet at <http://pubs.acs.org>.

■ AUTHOR INFORMATION

✉ Corresponding Author

*E-mail: fytas@mpip-mainz.mpg.de.

📍 Present Address

(K.I.J.) École Normale Supérieure, Département de Chimie, 24 rue Lhomond, 75231 Paris Cedex 05, France.

📝 Notes

The authors declare no competing financial interest.

■ ACKNOWLEDGMENTS

G.F. thanks the European Social Fund and the Greek Ministry of Education (GSRT) in the framework of the program THALIS for financial support.

■ REFERENCES

- (1) Dreaden, E. C.; Alkilany, A. M.; Huang, X. H.; Murphy, C. J.; El-Sayed, M. A. *Chem. Soc. Rev.* **2012**, *41*, 2740–2779.
- (2) Thakor, A. S.; Jokerst, J.; Zavaleta, C.; Massoud, T. F.; Gambhir, S. S. *Nano Lett.* **2011**, *11*, 4029–4036.
- (3) Pendry, J. *Science* **1999**, *285*, 1687–1688.
- (4) Maier, S. A.; Kik, P. G.; Atwater, H. A.; Meltzer, S.; Harel, E.; Koel, B. E.; Requicha, A. A. G. *Nat. Mater.* **2003**, *2*, 229–232.
- (5) Rosman, C.; Prasad, J.; Neiser, A.; Henkel, A.; Edgar, J.; Sonnichsen, C. *Nano Lett.* **2013**, *13*, 3243–3247.
- (6) Daniel, M. C.; Astruc, D. *Chem. Rev.* **2004**, *104*, 293–346.
- (7) Sun, Y. G.; Xia, Y. N. *Science* **2002**, *298*, 2176–2179.
- (8) Vigdeman, L.; Khanal, B. P.; Zubarev, E. R. *Adv. Mater.* **2012**, *24*, 4811–4841.

- (9) Mackay, M. E.; Tuteja, A.; Duxbury, P. M.; Hawker, C. J.; Van Horn, B.; Guan, Z. B.; Chen, G. H.; Krishnan, R. S. *Science* **2006**, *311*, 1740–1743.
- (10) Hui, C. M.; Pietrasik, J.; Schmitt, M.; Mahoney, C.; Choi, J.; Bockstaller, M. R.; Matyjaszewski, K. *Chem. Mater.* **2014**, *26*, 745–762.
- (11) Akcora, P.; Liu, H.; Kumar, S. K.; Moll, J.; Li, Y.; Benicewicz, B. C.; Schadler, L. S.; Acehan, D.; Panagiotopoulos, A. Z.; Pryamitsyn, V.; Ganesan, V.; Ilavsky, J.; Thiyagarajan, P.; Colby, R. H.; Douglas, J. F. *Nat. Mater.* **2009**, *8*, 354–359.
- (12) Gao, B.; Arya, G.; Tao, A. R. *Nat. Nanotechnol.* **2012**, *7*, 433–437.
- (13) Koerner, H.; Drummy, L. F.; Benicewicz, B.; Li, Y.; Vaia, R. A. *ACS Macro Lett.* **2013**, *2*, 670–676.
- (14) Hermans, T. M.; Broeren, M. A. C.; Gomopoulos, N.; van der Schoot, P.; van Genderen, M. H. P.; Sommerdijk, N. A. J. M.; Fytas, G.; Meijer, E. W. *Nat. Nanotechnol.* **2009**, *4*, 721–726.
- (15) Lane, J. M. D.; Grest, G. S. *Phys. Rev. Lett.* **2010**, *104*, 235501.
- (16) Salerno, K. M.; Ismail, A. E.; Lane, J. M.; Grest, G. S. *J. Chem. Phys.* **2014**, *140*, 194904.
- (17) Bozorgui, B.; Meng, D.; Kumar, S. K.; Chakravarty, C.; Cacciuto, A. *Nano Lett.* **2013**, *13*, 2732–2737.
- (18) Haghghi, M.; Plum, M. A.; Gantzounis, G.; Butt, H. J.; Steffen, W.; Fytas, G. *J. Phys. Chem. C* **2013**, *117*, 8411–8419.
- (19) Kelly, K. L.; Coronado, E.; Zhao, L. L.; Schatz, G. C. *J. Phys. Chem. B* **2003**, *107*, 668–677.
- (20) Piazza, R.; Degiorgio, V. *Phys. Rev. Lett.* **1991**, *67*, 3868–3871.
- (21) Portales, H.; Goubet, N.; Saviot, L.; Yang, P.; Sirotkin, S.; Duval, E.; Mermet, A.; Pileni, M. P. *ACS Nano* **2010**, *4*, 3489–3497.
- (22) Schubert, O.; Becker, J.; Carbone, L.; Khalavka, Y.; Provalska, T.; Zins, I.; Sonnichsen, C. *Nano Lett.* **2008**, *8*, 2345–2350.
- (23) Cang, H.; Montiel, D.; Xu, C. S.; Yang, H. *J. Chem. Phys.* **2008**, *129*, 044503.
- (24) Huang, W. Y.; Qian, W.; El-Sayed, M. A.; Ding, Y.; Wang, Z. L. *J. Phys. Chem. C* **2007**, *111*, 10751–10757.
- (25) Tang, Y.; Ouyang, M. *Nat. Mater.* **2007**, *6*, 754–759.
- (26) Schmidt, J. R.; Skinner, J. L. *J. Phys. Chem. B* **2004**, *108*, 6767–6771.
- (27) Koenderink, G. H.; Zhang, H. Y.; Aarts, D. G. A. L.; Lettinga, M. P.; Philipse, A. P.; Nagele, G. *Faraday Discuss.* **2003**, *123*, 335–354.
- (28) Berciaud, S.; Cognet, L.; Tamarat, P.; Lounis, B. *Nano Lett.* **2005**, *5*, 515–518.
- (29) Imabayashi, S.; Hobara, D.; Kakiuchi, T. *Langmuir* **2001**, *17*, 2560–2563.
- (30) Ionita, P.; Volkov, A.; Jeschke, G.; Chechik, V. *Anal. Chem.* **2008**, *80*, 95–106.
- (31) Hakkinen, H. *Nat. Chem.* **2012**, *4*, 443–455.
- (32) Ford, M. J.; Masens, C.; Cortie, M. B. *Surf. Rev. Lett.* **2006**, *13*, 297–307.